A Robust Two-Degree-of-Freedom Current Control Strategy for *LCL*-Equipped High-Speed PMSMs

Longhao Shi, Chenwen Cheng, Mingjin Hu, *Member, IEEE*, Wei Hua, *Senior Member, IEEE*, and Chunyu Lu

***Abstract*—For an inductor-capacitor-inductor (*LCL*) equipped high-speed permanent magnet synchronous machine (*LCL*-HSPMSM), the negative resonance frequency in the synchronous rotating frame poses a significant yet understudied challenge to the robustness of the adjustable-speed system. This article proposes a two-degree-of-freedom (2DOF) current control strategy that enhances the robustness of the system by maximizing its global stability margin. First, a mathematical model of an *LCL*-HSPMSM in the discrete-time domain is established, based on which the influence of both positive and negative resonance frequencies on the system stability is analyzed. Subsequently, a phase compensator and a phase gain are introduced to achieve active damping for both resonance frequencies. Additionally, a feedforward controller provides an extra DOF to mitigate the coupling between *dq*-axes currents, distinguishing it from the conventional control strategy. Consequently, a robust system resilient to parameter mismatches can be achieved. Finally, experimental verification of the robust control strategy is conducted on a 60kr/min *LCL*-HSPMSM prototype, where key parameters are varied from 0.3 to 3 times the nominal values.**

***Index Terms*—Complex vector, discrete time, feedforward, high-speed permanent magnet synchronous machine (HSPMSM), inductor-capacitor-inductor (*LCL*) filter, robustness, synchronous rotating frame (SRF).**

I. Introduction

HIGH-SPEED surface-mounted permanent magnet synchronous motors (HSPMSMs) are extensively employed in industrial applications due to their remarkable power density and efficiency. However, the small motor inductance results in significant current ripples, leading to additional power losses and torque ripples. To address this issue, an inductor-capacitor-inductor (*LCL*) filter can be implemented between the inverter and the motor as shown in Fig. 1. Nevertheless, the high-order nature of the *LCL* filter significantly increases system complexity, posing challenges for the controller design. In particular, the resonance peak introduced by the *LCL* circuit potentially affects the stability of the current control loop [1], [2]. Moreover, the system parameters vary widely in different operating conditions, demanding strong parameters robustness for the controller design.

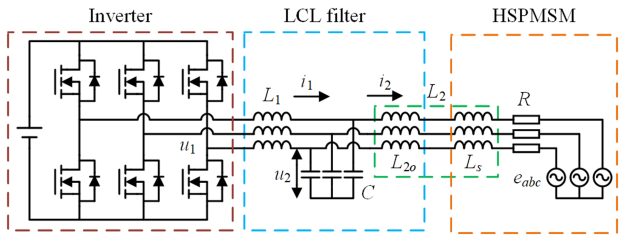

Fig. 1. System diagram of the *LCL*-HSPMSM system.

Considerable research efforts have been dedicated to the development of active damping (AD) strategies to effectively address the resonance issue, which can be concluded as resonant pole cancelation [3], [4], [5], [6], virtual-resistance [7], [8], [9], [10], [11], full-state feedback control (FSFC) [12], [13], [14], [15], [16], and filter-based damping [17], [18], [19], [20], [21].

Resonant pole cancelation methods include the notch filter [3], weighted average current (WAC) control [4], and capacitor voltage feedback [5]. A cascade notch filter is a straightforward method to cancellate the resonance pole by setting the notch frequency exactly at the resonance frequency. The resonant pole can also be cancellated by the reasonable configuration of weight facts of WAC or the capacitor feedback coefficient. However, these methods require the exact value of resonance frequency, when parameter mismatch occurs, the damping effects will deteriorate seriously, indicating weak robustness [6].

The virtual-resistance AD method is popularly used, which is mainly achieved by the proportional capacitor current feedback [7], [8]. However, the effectiveness of this method is highly degraded by the inherent digital computation delay. To address this issue, some improvements were employed by reducing computational delay [9] or modifying the feedback strategy [10], [11]. Nevertheless, the robustness is still limited, and the requirement for the additional capacitor current measurement leads to extra costs.

The FSFC method can achieve robustness through arbitrary pole assignment [12], [13]. However, this approach necessitates the costly measurement of all states. Introducing a state observer allows for the implementation of full state feedback with just a single sensor [14], [15]. Furthermore, a single-sensor damping

Received 22 May 2024; revised 17 July 2024; accepted 24 August 2024. Date of publication 27 August 2024; date of current version 7 October 2024. This work was supported by the National Natural Science Foundation of China under Grant 52307044. Recommended for publication by Associate Editor J. Ye. *(Corresponding author: Chenwen Cheng.)*

The authors are with the School of Electrical Engineering, Southeast University, Nanjing 210096, China (e-mail: 220222733@seu.edu.cn; chenwen_cheng@seu.edu.cn; hmj@seu.edu.cn; huawei1978@seu.edu.cn; 220202873@seu.edu.cn).

Color versions of one or more figures in this article are available at https://doi.org/10.1109/TPEL.2024.3450748.

Digital Object Identifier 10.1109/TPEL.2024.3450748

framework is introduced, enabling equivalent arbitrary pole assignment with a single sensor without the need for an observer [16]. Nevertheless, these methods heavily rely on system parameters, and parameter mismatch can degrade the system's robustness, especially with a state observer.

The filter-based damping methods seem to be a proper way to achieve high parameters robustness because the controller design is relatively insensitive to the system parameters. For the motor side current or grid side current feedback system, the resonance is damped by introducing an additional phase lag in the resonance frequency. Various methods are employed to achieve this goal, including the use of first-order low-pass filters (LPF),∗ second-order LPF [17], and the introduction of additional delay [18]. Additionally, the notch filter can also serve as an LPF due to its phase lag characteristic to the left of the notch frequency [19].

Overall, the aforementioned methods are primarily established in the stationary coordinate for grid-connected applications. For the *LCL*-HSPMSM system, the motor current controller is usually designed in the synchronous rotating frame (SRF) to enhance the current transient performance. In this configuration, the natural resonance frequency is transformed into two resonance values, located at $f_{\rm res}$-f_e and $f_{\rm res}$+f_e (where $f_{\rm res}$ is the natural resonance frequency and f_e is the electrical frequency). However, in the existing filter-based damping methods [20], [21] only the positive resonance frequency is considered, and the underestimation of the negative resonance frequency may lead to stability issues.

On the other hand, traditional proportional-integral (PI) controllers and filter-based damping methods are typically classified as one degree of freedom (1DOF) controllers because they rely solely on the error between the reference and feedback values. This single DOF limits the controller's ability to independently design and optimize reference tracking performance and disturbance rejection performance. To overcome this limitation, several 2DOF control strategies have been developed. These strategies enhance various aspects of control performance. For instance, strategies such as the one proposed in [22] and [23] to improve the reference tracking performance under certain conditions such as sensorless control or current harmonic suppression, while methods like those in [23] focus on minimizing the impact of external disturbances on the system's output. Furthermore, approaches described in [16], [24], and [25] allow for more flexible placement of system poles and zeros, thereby tailoring the overall performance of the system. In these 2DOF control strategies, the second DOF is often implemented through a feedforward controller, a disturbance observer, or a combination of both. This additional degree of freedom enables a more versatile control design that can handle multiple performance criteria simultaneously.

This article conducts a comprehensive analysis of the influence of the negative resonance frequency. A global phase margin is defined to characterize the overall stability considering the presence of the negative resonance frequency. Accordingly, several efforts have been made to enhance the global stability margin.

TABLE I
CRITICAL PARAMETERS OF THE *LCL*-HSPMSM SYSTEM

Symbol	Parameter	Value
R	Winding resistance	0.02 Ω
L_1	Inductance at the inverter side	60 uH
L_{2o}	Inductance at the machine side	50 uH
L_s	Inductance of the machine	11 uH
C	Capacitor of *LCL* filter	60 uF
f_{res}	Resonance frequency	3736 Hz
U_{dc}	DC bus voltage	60 V
f_s	Sampling frequency	15 kHz
f_{sw}	Switching frequency	15 kHz
ψ_f	Flux linkage	1.02 mWb
P_r	Pole pairs	1
n_N	Rated speed	60000 rpm
f_e	Rated electrical frequency	1000 Hz
P_N	Rated power	500 W

First, a phase compensator is designed in the stationary frame and applied in the SRF, providing consistent phase lag at both resonance frequencies. Second, a phase gain is introduced to enhance the global stability margin, considering both resonance frequencies. Furthermore, a feedforward controller is introduced to address the additional coupling effects caused by the phase gain, forming a 2DOF control system. Different from the aforementioned 2DOF control strategies, the proposed 2DOF strategy utilizes the additional degree of freedom (feedforward controller) specifically to address the coupling effects in the dynamic response in the *dq*-axis caused by the phase gain.

As the main contribution, the potential stability issue associated with the dual resonance issue in the filter-based damping method is highlighted, especially in high-speed conditions. To tackle this challenge, a novel AD strategy is introduced, aimed at maximizing the global phase margin while taking into account the dual resonance problem. Consequently, this approach significantly enhances the overall robustness of the system.

Finally, the effectiveness of the proposed control strategy is validated by driving the test HSPMSM up to 60 kr/min (1000 Hz) with a sampling frequency of 15 kHz. Robustness is validated in the experiment with all system parameters varying from 0.3 to 3 times their nominal values. A comprehensive comparison with recently proposed damping methods is performed, further indicating the high robustness of the proposed method.

II. STABILITY ANALYSIS BASED ON DISCRETE-TIME MODEL

This section presents the discrete-time domain model of the *LCL*-HSPMSM system. The diagram of the system is depicted in Fig. 1, comprising a three-phase inverter, an *LCL* filter, and an HSPMSM. The inverter side inductor is defined as L_1. The filtering capacitor is defined as C. And the motor side inductor is defined as L_2, which consists of the filter inductor $L_{2\,o}$ and the motor inductor L_s. R is the winding resistance. All parameters are outlined in Table I, and these parameters are utilized in the analysis presented in this article as well as in the experiments in Section VI. Finally, Section VII concludes this article.

A. Discrete Model

The continuous-time transfer function from the inverter voltage to the motor current in the stationary frame can be derived as

$$G_{ps}(s)=\frac{i_2(s)}{u_1(s)}=\frac{1}{R+(L_1+L_2)s+L_1CRs^2+L_1L_2Cs^3}. \tag{1}$$

Since the motor resistance is included, the explicit symbolic expression of this discrete-time model is difficult to obtain. Numerical results can be computed based on specific parameters for robust analysis. However, for the controller design, the model should be simplified. Typically, the winding resistance is disregarded due to its minor impact on the system's characteristics at high frequencies [19], [27]. The simplified model is given as

$$\begin{aligned} &G_{ps}(s)\approx G^*_{psl}(s)+G_{psh}(s)\\ &G^*_{psl}(s)=\frac{1}{(L_1+L_2)s},\ G_{psh}(s)=-\frac{1}{L_1+L_2}\frac{s}{s^2+\omega_{\text{res}}^2} \end{aligned} \tag{2}$$

where $G^*_{psl}(s)$ and $G_{psh}(s)$ are the low-frequency and high-frequency components of the transfer function, and $\omega_{\text{res}}=2\pi\ f_{\text{res}}=\sqrt{(L_1+L_2)/(L_1L_2C)}$ is the natural resonance frequency.

In the controller design, the current control bandwidth typically aligns with the low-frequency band (LFB). Thus, a more accurate model in the LFB is imperative to improve the accuracy of the zero-pole cancellation in the discrete-time PI controller design, which enhances the dynamic performance of the control system, especially the dynamic decoupling capability of the response in the *dq*-axes. Accordingly, the effects of the motor resistance in the LFB are reconsidered. The modified low-frequency transfer function is given as

$$G_{psl}(s)=\frac{1}{R+(L_1+L_2)s}. \tag{3}$$

By discretizing the separated model with the zero-order hold method, an accurate model with delay can be obtained by

$$G_{ps}(z)=z^{-1}(G_{psl}(z)+G_{psh}(z)) \tag{4}$$

where

$$\begin{aligned} G_{psl}(z)&=\frac{1-e^{-\frac{R}{L_1+L_2}T_s}}{R}\frac{1}{z-e^{-\frac{R}{L_1+L_2}T}}\\ G_{psh}(z)&=-\frac{(z-1)\sin(\omega_{\text{res}}T)}{\omega_{\text{res}}(L_1+L_2)\left(z^2-2z\cos(\omega_{\text{res}}T)+1\right)}. \end{aligned} \tag{5}$$

Further, the transfer function $G_p(z)$ in the SRF can be developed by applying the frequency shift $z\rightarrow ze^{j\omega_eT}$, which leads to

$$G_p(z)=z^{-1}e^{-j\omega_eT}(G_{pl}(z)+G_{ph}(z)) \tag{6}$$

where

$$G_{pl}(z)=\frac{1-e^{-\frac{R}{L_1+L_2}T_s}}{R}\frac{1}{ze^{j\omega_eT}-e^{-\frac{R}{L_1+L_2}T}}$$

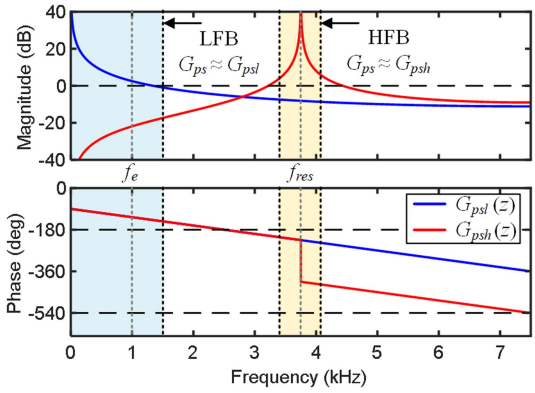

Fig. 2. Bode diagrams of $G_{psl}(z)$ and $G_{psh}(z)$ in the stationary frame ($f_e=1000$ Hz).

$$G_{\text{ph}}(z)=-\frac{(ze^{j\omega_eT}-1)\sin(\omega_{\text{res}}T)}{\omega_{\text{res}}(L_1+L_2)\left(z^2e^{2j\omega_eT}-2ze^{j\omega_eT}\cos(\omega_{\text{res}}T)+1\right)}. \tag{7}$$

Significantly, the amplitudes of the two transfer functions in their respective frequency bands far surpass each other. As depicted in Fig. 2, within the LFB, the plant model can be effectively simplified as $G_{pl}(z)$, while within the high-frequency band (HFB), the plant model can be similarly simplified as $G_{\text{ph}}(z)$. Consequently, these bands can be addressed separately during the controller design process. Additionally, for HSPMSMs, despite the relatively higher electrical frequency f_e, it can still be regarded within the LFB with respect to the resonance frequency.

B. Discrete PI Controller

As mentioned earlier, the plant model G_p can be simplified as G_{pl} in the LFB. Considering further that the current control bandwidth is significantly lower than the resonance frequency and the electrical frequency is high for the HSPMSM, a PI controller directly designed in the discrete-time domain based on the internal model decoupling theory is employed to enhance the current control performance in high-speed conditions [28]. The controller is expressed as

$$\begin{aligned} G_c(z)&=\left(G_{pl}(z)z^{-1}e^{-j\omega_eT}\right)^{-1}\frac{K}{z(z-1)}\\ &=\lambda\frac{ze^{j\omega_eT}-\delta}{z-1}Ke^{j\omega_eT} \end{aligned} \tag{8}$$

where

$$\delta=e^{-\frac{R}{L_1+L_2}T},\ \lambda=\frac{R}{1-e^{-\frac{R}{L_1+L_2}T_s}} \tag{9}$$

and K is the gain of the controller.

C. Stabilities in Positive and Negative Frequency Domains

The stability of the *LCL* system is typically evaluated by the Nyquist stability criterion based on the Bode diagram or Nyquist plot. According to this theory, the system is stable when the number of the open-loop unstable poles P is equal to $2(N_+\text{-}N\text{-})$, where N_+ represents the number of counterclockwise

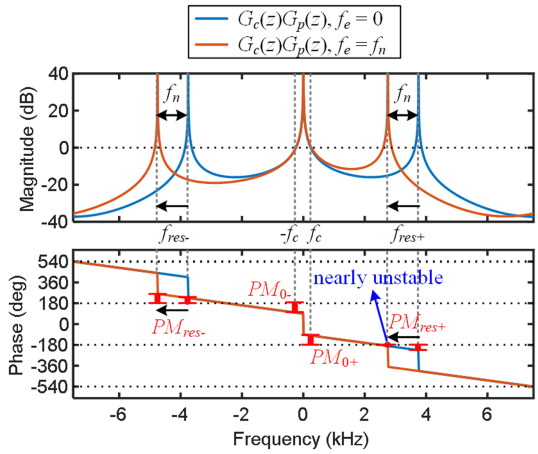

Fig. 3. Bode diagram of $G_c(z)G_p(z)$ in both positive and negative frequency domains with speed variation. The length of the red lines represents the values of different phase margins ($f_n = 1000$ Hz, $K = 0.1$. The winding resistance is ignored in the HFB).

encirclements of the point (-1, *j*0) in the complex plane as the frequency ranges from -f_s/2 to f_s/2, and N_- represents the number of clockwise encirclements [18]. For the motor current feedback system, it can be seen from (1) that $P = 0$. Thus, to ensure system stability, it is required that $N_+ - N_- = 0$, which means there should be no phase crossing of $(2k+1)\pi$ in the frequency regions where the magnitudes are above 0 dB.

In the stationary frame, the magnitude response is symmetric in both positive and negative frequency domains. Therefore, it is sufficient to analyze resonance stability by focusing solely on the positive frequency domain. However, in the SRF, the transfer function in (7) contains complex coefficients that disrupt the symmetry in the frequency domain. This issue becomes particularly significant under high-speed conditions due to the larger resonance frequency shift as illustrated in Fig. 3, which shows the bode diagram of $G_c(z)G_p(z)$. As f_e increases, the bode plots shift to the left and lose their symmetry. Therefore, in the SRF, there are two different resonant frequencies: $f_{\mathrm{res}+} = f_{\mathrm{res}} - f_e$ and $f_{\mathrm{res}-} = f_{\mathrm{res}} + f_e$.

As mentioned earlier, the system is stable when the phase response avoids crossing the $(2k\text{-}1)\pi$ phase line in the frequency regions where the magnitudes are above 0 dB. In summary, the stability issue should encompass three frequency regions: two resonance frequencies and their vicinities, along with a low-frequency region spanning from $-f_c$ to $+f_c$, where f_c represents the 0dB crossing frequency in the LFB. It is worth noting that the resonance frequency regions are relatively small, especially when considering the influence of winding resistance. Therefore, for the sake of simplicity, stability analysis in the HFB primarily focuses on the resonance frequencies.

In the aforementioned three regions, any crossing of the $(2k\text{-}1)\pi$ phase line signifies instability in the system. Thus, to quantify the global system stability margin, four types of phase margins (PMs) are first introduced.

1) PM_{0+}: PM at positive 0 dB crossing frequency f_c.
2) PM_{0-}: PM at negative 0 dB crossing frequency $-f_c$.
3) $\mathrm{PM}_{\mathrm{res}+}$: PM at positive resonance frequency $f_{\mathrm{res}+}$.
4) $\mathrm{PM}_{\mathrm{res}-}$: PM at negative resonance frequency $f_{\mathrm{res}-}$.

Additionally, the PMs in the LFB and HFB can be respectively defined as

$$\begin{aligned} \mathrm{PM}_0 &= \min\{\mathrm{PM}_{0-}, \mathrm{PM}_{0+}\} \\ \mathrm{PM}_{\mathrm{res}} &= \min\{\mathrm{PM}_{\mathrm{res}-}, \mathrm{PM}_{\mathrm{res}+}\}. \end{aligned} \tag{10}$$

All of the above PMs are illustrated in Fig. 3 for reference. Based on the setup in Table I, the values of these four PM_s are given as

$$\begin{aligned} &\mathrm{PM}_{0-} = 81.4^\circ, \mathrm{PM}_{0+} = 81^\circ \\ &\mathrm{PM}_{\mathrm{res}+} = \begin{cases} 45^\circ, f_e = 0 \text{ Hz} \\ 9^\circ, f_e = 1000 \text{ Hz} \end{cases} \\ &\mathrm{PM}_{\mathrm{res}-} = \begin{cases} 45^\circ, f_e = 0 \text{ Hz} \\ 80^\circ, f_e = 1000 \text{ Hz} \end{cases}. \end{aligned} \tag{11}$$

Among these four PM values, a low value would lead to a decrease in the system's stability margin, resulting in a deterioration of stability and control performance. Especially, if any of them is equal to 0, the system will be unstable. Thus, the global phase margin is defined as

$$\mathrm{PM}_{\min} = \min\{\mathrm{PM}_{0-}, \mathrm{PM}_{0+}, \mathrm{PM}_-, \mathrm{PM}_+\}. \tag{12}$$

$\mathrm{PM}_{\min}$ is a more concise metric to represent the global stability margin of the system, and the method to achieve the maximum $\mathrm{PM}_{\min}$ will be analyzed in detail in this article.

Furthermore, it is evident from Fig. 3 that as the electrical frequency f_e increases, $\mathrm{PM}_{\mathrm{res}+}$ decreases, while $\mathrm{PM}_{\mathrm{res}-}$ increases; PM_{0+} and PM_{0-} remain consistent. Consequently, $\mathrm{PM}_{\min}$ decreases due to the low $\mathrm{PM}_{\mathrm{res}+}$, necessitating the implementation of AD.

D. Limitations of Existing Damping Methods

Given that the $\mathrm{PM}_{\min}$ is primarily determined by $\mathrm{PM}_{\mathrm{res}+}$, various filter-based damping methods have been proposed to reduce the phase at $f_{\mathrm{res}+}$ [18], [19], [20]. However, these methods could simultaneously affect the phase at $f_{\mathrm{res}-}$, potentially leading to stability problems, particularly under high electrical frequency conditions.

Fig. 4 illustrates the phase plots of the existing damping methods and their damping effects, including a notch filter [19], [20], and an additional delay [18]. The notch frequency of the notch filter is designed as $\omega_n = 1.3\omega_{\mathrm{res}}$ to provide phase lag in $f_{\mathrm{res}+}$. The additional delay is applied in the stationary frame, where its equivalent transfer function in the SRF is $z^{-1}e^{-j\omega_e T}$.

First, regarding damping methods with an additional delay, it will introduce a 90° phase lag in $f_{\mathrm{res}+}$, effectively damping the resonance. However, simultaneously, the additional delay introduces a significant phase lead of 90° at $f_{\mathrm{res}-}$ within the negative frequency domain. In that case, the phase at $f_{\mathrm{res}-}$ closely approaches the $(2k\text{-}1)\pi$ line (540°) resulting in a $\mathrm{PM}_{\min}$ as low as 9°, indicating a weak stability.

Similarly, the notch filter could add an extra phase lag of 28° at the positive resonance frequency $f_{\mathrm{res}+}$ to perform AD. However, a substantial phase lag of 75° is also introduced by the notch filter, leading to a $\mathrm{PM}_{\min}$ as low as 5°.

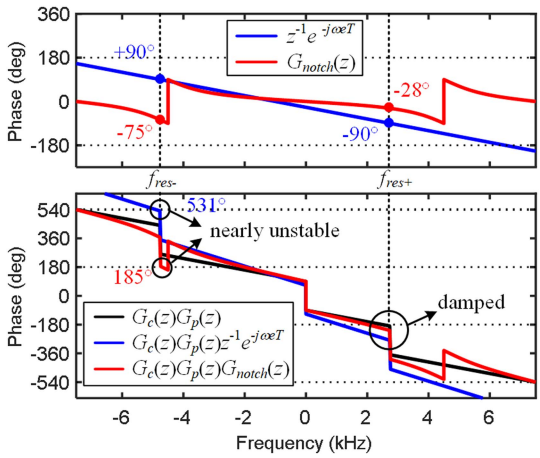

Fig. 4. Phase-frequency response of existing damping methods with $f_e = 1000$ Hz.

In conclusion, both damping methods exhibit very small $\mathrm{PM}_{\min}$ values, indicating weak system robustness. An effective way is required to achieve AD for both resonance frequencies.

III. Active Damping for Dual Resonance Issues

In this section, an AD control strategy is presented to address the dual resonance issue discussed earlier, including three parts.

1) A phase compensator designed in the stationary frame and applied in the SRF.
2) A phase gain to provide a global stability margin.
3) A feedforward controller to decouple the coupling issues caused by the phase gain, serving as the second DOF.

The primary objective of this damping strategy is to ensure an adequate global stability margin within the closed-loop system while effectively achieving decoupling through the inversion of the closed-loop transfer function in the feedforward decoupling controller. The overall control strategy is depicted in Fig. 5.

A. Phase Compensator

The phase compensator is designed to ensure consistent phase lag at both resonance frequencies, necessitating its design in the stationary frame. It is derived from a first-order LPF using the pretwisted bilinear transformation method for discretization, known for its ability to preserve unchanged phase characteristics at resonance frequencies [29], given as

$$G_{pcs}(z) = \frac{\omega_{lpf}}{s+\omega_{lpf}}\left(s = \frac{\omega_{\mathrm{res}}}{\tan(\frac{\omega_{\mathrm{res}}T}{2})}\frac{z-1}{z+1}\right) = \frac{z+1}{(1+\alpha)z+1-\alpha}\left(\alpha = \frac{\omega_{\mathrm{res}}}{\omega_{lpf}\tan\left(\frac{\omega_{\mathrm{res}}T}{2}\right)}\right). \tag{13}$$

The equivalent transfer function in the SRF is derived by applying the frequency shift $z \to ze^{j\omega_e T}$, given as

$$G_{pc}(z) = G_{pcs}\left(ze^{j\omega_e T}\right) = \frac{ze^{j\omega_e T}+1}{(1+\alpha)ze^{j\omega_e T}+1-\alpha}. \tag{14}$$

The effects of the phase compensator are illustrated in Fig. 6. The phase response decreases at $f_{\mathrm{res}+}$ and increases at $f_{\mathrm{res}-}$. Unlike the filters designed in the SRF (analyzed in Section II-D), the phase compensator can deliver consistent phase changes at both resonance frequencies. Consequently, it effectively addresses potential stability issues at the negative resonance frequency. Consequently, when $\mathrm{PM}_{\mathrm{res}+}$ increases, $\mathrm{PM}_{\mathrm{res}-}$ decreases, with little change observed in PM_0. This leads to an overall enhancement of the global phase margin.

On the basis of the phase compensator, the global phase margin of the system can be further enhanced by introducing a series phase gain, which is given as

$$G_{pg}(z) = e^{j\varphi} \tag{15}$$

where φ is the global phase shift angle.

With the phase gain, the entire phase curve can be shifted up or down by the value of φ. For example, as shown in Fig. 7, when φ is negative, the phase-frequency curve shifts downward as a whole. It can be found that as the phase gain decreases, $\mathrm{PM}_{\mathrm{res}}$ increases, while PM_0 decreases.

B. Phase Gain

As $\mathrm{PM}_{\min}$ is determined by the minimum phase margin among all components, by reasonably setting the phase gain, it is possible to ensure that PM_0 and $\mathrm{PM}_{\mathrm{res}}$ remain identical, thereby maximizing the global system margin.

C. Feedforward Decoupling Controller

In the above design, the additional phase compensator and phase gain are all complex vector controllers, which will cause additional coupling issues [30]. Therefore, a feedforward decoupling controller is proposed to achieve dynamic decoupling by inverting the closed-loop transfer function of the system. The specific expression is as follows:

$$\begin{aligned} G_{ff}(z) &= G_{\mathrm{close}}^{-1}(z)\frac{K_f}{z^2-z+K_f} \\ &= \frac{1+G_{pg}(z)G_{\mathrm{inv}}(z)G_{pc}(z)G_p(z)}{G_{pg}(z)G_{inv}(z)G_{pc}(z)G_p(z)}\frac{K_f}{z^2-z+K_f} \\ &= \frac{K_f}{K}e^{-j\varphi}((1+\alpha)+((1-\alpha)e^{-j\omega_e T}-(1+\alpha))z^{-1} \\ &\quad +((\alpha-1)e^{-j\omega_e T}+Ke^{j\varphi})z^{-2}+Ke^{j\varphi-j\omega_e T}z^{-3})/ \\ &\quad (1+(e^{-j\omega_e T}-1)z^{-1}+(K_f-e^{-j\omega_e T})z^{-2} \\ &\quad +K_f e^{-j\omega_e T}z^{-3}) \end{aligned} \tag{16}$$

where K_f represents the feedforward gain of the system.

IV. Parameter Determination Procedure

This section describes the parameter design procedure for the proposed control strategy, aiming at maximizing the stability margin while ensuring dynamic performance.

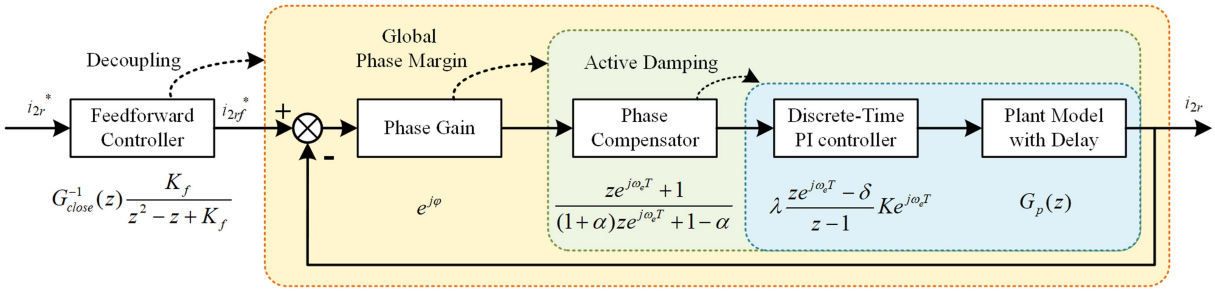

Fig. 5. Block diagram of the proposed 2DOF current control strategy.

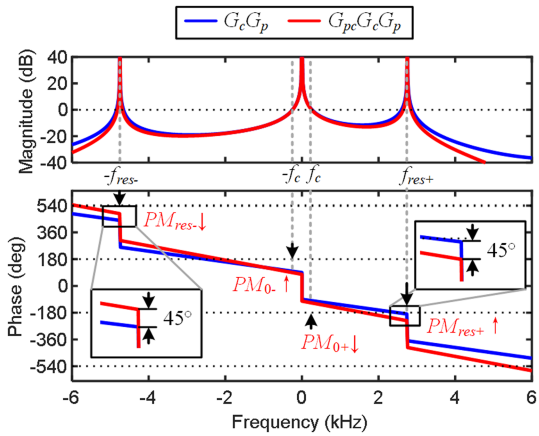

Fig. 6. Frequency response variation with phase compensator ($f_e = 1000$ Hz, $K = 0.05$, $\alpha = 2$).

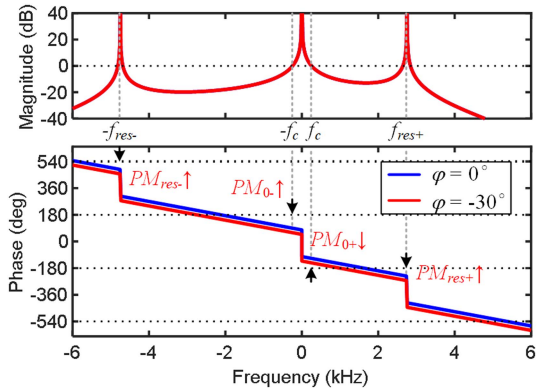

Fig. 7. Frequency response variation of the open-loop transfer function $G_{pg}(z)G_{pc}(z)G_c(z)G_p(z)$ with phase compensator ($f_e = 1000$ Hz, $K = 0.05$, and $\alpha = 2$).

A. Phase Compensator

The phase compensator is designed to induce a phase lag at the resonance frequency within the range of $-180°$ to $-540°$. In the following, the phase of $G_{ps}(z)$ at the resonance frequency is first calculated. Accordingly, the coefficient α of the phase compensator is further determined.

As aforementioned, at the resonance frequency, the amplitude of the low-frequency transfer function is negligible. Thus, the phase at the resonance frequency can be directly obtained based on the high-frequency transfer function, which is given as

$$\begin{aligned}&\angle G_{ps}(e^{j\omega_{res}T})(\omega \to \omega_{\text{res}-})\\&= \arctan 2(\sin(\omega_{res}T), \cos(\omega_{res}T) - 1) - 2\omega_{\text{res}}T - \pi\\&\angle G_{ps}(e^{j\omega_{res}T})(\omega \to \omega_{\text{res}-})\\&= \arctan 2(\sin(\omega_{res}T), \cos(\omega_{res}T) - 1) - 2\omega_{\text{res}}T - 2\pi.\end{aligned} \tag{17}$$

The design objective of the phase compensator is to control the phase shift to be from -1.5π to -2.5π. Thus, the phase lag to be compensated is calculated as

$$\begin{aligned}\varphi_{pc} &= \angle G_{pc}(z)(z = e^{j\omega_{\text{res}}T})\\&= -\arctan 2(\sin(\omega_{\text{res}}T), \cos(\omega_{\text{res}}T) - 1) + 2\omega_{\text{res}}T - \frac{\pi}{2}.\end{aligned} \tag{18}$$

Next, based on the required phase shift, the bandwidth of the first-order low-pass filter is calculated as

$$\omega_{lpf} = \omega_{\text{res}} / \tan(\varphi_{pc}). \tag{19}$$

The corresponding coefficient can be calculated as

$$\alpha = \frac{\omega_{\text{res}}}{\omega_{lpf}\tan(\frac{\omega_{\text{res}}T}{2})} = \frac{\tan(\varphi_{pc})}{\tan(\frac{\omega_{\text{res}}T}{2})}. \tag{20}$$

B. Feedforward Gain and Closed-Loop Gain

The gain of the system determines its bandwidth and further affects system stability, dynamic performance, and anti-disturbance performance. This section will discuss the selection of the closed-loop gain K and the feed-forward gain K_f from these considerations.

Ignoring the influence of phase compensator and high-frequency resonance, the closed-loop transfer function and follow-up response transfer function of the system can be expressed as

$$G_{\text{close}}(z) = \frac{i(z)}{i_{ff}^*(z)} = \frac{K}{z^2 - z + K} \tag{21}$$

$$G_{\text{ref}}(z) = \frac{i(z)}{i^*(z)} = \frac{K_f}{z^2 - z + K_f}. \tag{22}$$

Equation (22) indicates that the following response of the system is only related to the feedforward gain K_f. By increasing K_f, the dynamic response of the system can be effectively improved. However, an excessively large feedforward gain makes

the system more susceptible to the influence of voltage saturation, leading to issues, such as overshooting and coupling.

On the other hand, the closed-loop gain K determines the bandwidth of the closed-loop system and further affects PM_0. A larger K results in a lower PM_0. It also increases the amplitude at the resonance frequency, expanding the frequency range above the 0dB line and reducing the stability margin.

As a reference, ignoring the phase compensator, the 0dB crossing frequency can be approximately simplified as

$$\omega_{b-\mathrm{close}} \approx \frac{K}{T}. \tag{23}$$

In summary, considering the system stability and dynamic performance, the recommended values for the feedforward gain and feedback gain are

$$K = 0.05, K_f = 0.1. \tag{24}$$

In practical applications, corresponding adjustments can be made according to requirements.

C. Phase Gain

In this section, numerical calculation of four phase margins will be performed, including PM_{0+}, PM_{0-}, $\mathrm{PM}_{\mathrm{res}+}$, $\mathrm{PM}_{\mathrm{res}-}$. The effects of the phase gain to maximize the global system margin will be explained in detail.

1) Phase Margins in the LFB: In the LFB, the open-loop transfer function can be simplified as

$$\begin{aligned} G_l(z) &= G_c(z)G_p(z)G_{pc}(z) \\ &\approx G_c(z)z^{-1}e^{-j\omega_e T}G_{pl}(z)G_{pc}(z) \\ &= \frac{K}{z^2 - z}G_{pc}(z) \end{aligned} \tag{25}$$

where

$$\angle \frac{K}{z^2 - z}\left(z = e^{j\omega T}\right) = -\frac{\pi}{2} - \frac{3}{2}\omega T. \tag{26}$$

The phase of the phase compensator can be approximately linearized as

$$\angle G_{pc}(z)(z = e^{j\omega T}) \approx -\left(\omega + \omega_e\right)\frac{\varphi_{pc}}{\omega_{res}}. \tag{27}$$

Accordingly, PM_0 can be calculated as

$$\mathrm{PM}_{0+} = \frac{\pi}{2} - \frac{3}{2}\omega_b T - \frac{\omega_b}{\omega_{\mathrm{res}}}\varphi_{pc} - \frac{\omega_e}{\omega_{\mathrm{res}}}\varphi_{pc} + \varphi \tag{28}$$

$$\mathrm{PM}_{0-} = \frac{\pi}{2} - \frac{3}{2}\omega_b T - \frac{\omega_b}{\omega_{\mathrm{res}}}\varphi_{pc} + \frac{\omega_e}{\omega_{\mathrm{res}}}\varphi_{pc} - \varphi. \tag{29}$$

Based on (28) and (29), the phase margin in the LFB is calculated as

$$\begin{aligned} \mathrm{PM}_0 &= \min\{\mathrm{PM}_{0+}, PM_{0-}\} \\ &= \frac{\pi}{2} - \frac{3}{2}\omega_b T - \frac{\omega_b}{\omega_{\mathrm{res}}}\varphi_{pc} - |\varphi - \frac{\omega_e}{\omega_{\mathrm{res}}}\varphi_{pc}|. \end{aligned} \tag{30}$$

2) Phase Margins in the HFB: In the HFB, the open-loop transfer function can be simplified as

$$G_h(z) \approx G_c(z)G_{pc}(z)z^{-1}e^{-j\omega_e T}G_{ph}(z). \tag{31}$$

As aforementioned about the phase compensator, the phase of the plant model series with phase compensator is

$$\begin{aligned} \angle G_p(z)G_{pc}(z)\left(z = e^{j\omega_{\mathrm{res}-}T}\right) &= -\frac{3}{2}\pi \\ \angle G_p(z)G_{pc}(z)\left(z = e^{j\omega_{\mathrm{res}+}T}\right) &= -\frac{5}{2}\pi. \end{aligned} \tag{32}$$

Considering that δ is generally close to 1. The PI controller can be simplified as

$$G_c(z) \approx \lambda K\frac{e^{j(\omega+\omega_e)T} - 1}{e^{j\omega T} - 1}Ke^{j\omega_e T}. \tag{33}$$

The phase of the controller at the resonance frequencies can be calculated as

$$G_c(z)\left(z = e^{j\omega_{\mathrm{res}}T}\right) \approx \frac{3}{2}\omega_e T, G_c(z)\left(z = e^{-j\omega_{\mathrm{res}}T}\right) \approx -\frac{3}{2}\omega_e T. \tag{34}$$

Thus, the phase margin in the HFB is introduced as

$$\mathrm{PM}_{\mathrm{res}} = \mathrm{PM}_{\mathrm{res}+} = \mathrm{PM}_{\mathrm{res}-} = \frac{\pi}{2} - \frac{3}{2}\omega_e T - \varphi. \tag{35}$$

The total phase margin of the resonance frequency is

$$\mathrm{PM}_{\mathrm{res}} = \min\{\mathrm{PM}_{\mathrm{res}+}, \mathrm{PM}_{\mathrm{res}-}\} = \frac{\pi}{2} - \frac{3}{2}\omega_e T - \varphi. \tag{36}$$

3) Determination of the Phase Gain: Based on the previous calculations in (30) and (36), the effect of the phase gain can be concluded as

$$\begin{aligned} &\varphi < \frac{\varphi_{pc}}{\omega_{\mathrm{res}}}\omega_e, \varphi \uparrow, \mathrm{PM}_0 \uparrow, \mathrm{PM}_{\mathrm{res}} \downarrow \\ &\varphi > \frac{\varphi_{pc}}{\omega_{\mathrm{res}}}\omega_e, \varphi \uparrow, PM_0 \downarrow, \mathrm{PM}_{\mathrm{res}} \downarrow . \end{aligned} \tag{37}$$

The PM in both frequency bands can be expressed as

$$\begin{aligned} \mathrm{PM}_0 = PM_{0+} &= \frac{\pi}{2} - \frac{3}{2}\omega_b T - \frac{\omega_b}{\omega_{\mathrm{res}}}\varphi_{pc} - \frac{\omega_e}{\omega_{\mathrm{res}}}\varphi_{pc} + \varphi \\ \mathrm{PM}_{\mathrm{res}} &= \frac{\pi}{2} - \frac{3}{2}\omega_e T - \varphi \left(\varphi \le \frac{\omega_e}{\omega_{\mathrm{res}}}\varphi_{pc}\right). \end{aligned} \tag{38}$$

To achieve the maximum global phase margin $\mathrm{PM}_{\min} = \min\{\mathrm{PM}_0, \mathrm{PM}_{\mathrm{res}}\}$, the phase gain is selected as

$$\varphi = \begin{cases} \frac{\omega_e}{\omega_{\mathrm{res}}}\varphi_{pc}, \omega_e < \omega_b \\ -\frac{3}{4}\omega_e T + \frac{3}{4}\omega_b T + \frac{\omega_b}{2\omega_{\mathrm{res}}}\varphi_{pc} + \frac{\omega_e}{2\omega_{\mathrm{res}}}\varphi_{pc}, \omega_e > \omega_b \end{cases}. \tag{39}$$

Accordingly, the global phase margin is calculated as

$$\mathrm{PM}_{\min} = \begin{cases} \frac{\pi}{2} - \frac{3}{2}\omega_b T - \frac{\omega_b}{\omega_{\mathrm{res}}}\varphi_{pc}, \omega_e < \omega_b \\ \frac{\pi}{2} - (\omega_e + \omega_b)(\frac{3}{4}T + \frac{\varphi_{pc}}{\omega_{\mathrm{res}}}), \omega_e > \omega_b \end{cases}. \tag{40}$$

In conclusion, the global phase margin is determined by the electrical frequency and the closed-loop bandwidth. In the low-speed range ($\omega_e < \omega_b$), $\mathrm{PM}_{\mathrm{res}}$ is larger than PM_0, and the global phase margin depends on PM_0. As the speed increases, $\mathrm{PM}_{\mathrm{res}}$ gradually decreases. When $\omega_e > \omega_b$, $\mathrm{PM}_{\mathrm{res}}$ is smaller than PM_0. By incorporating the phase gain, the balance of $\mathrm{PM}_{\mathrm{res}}$ and PM_0 can be achieved.

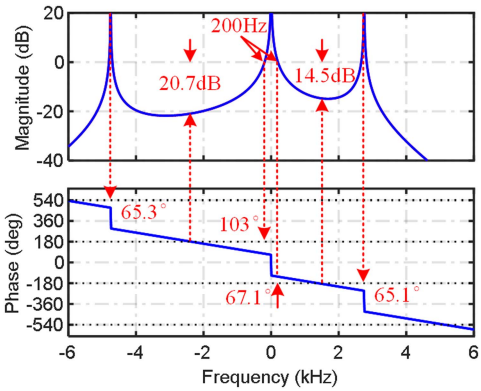

Fig. 8. Bode plots of the designed system ($f_e = 1$ kHz and $f_s = 15$ kHz).

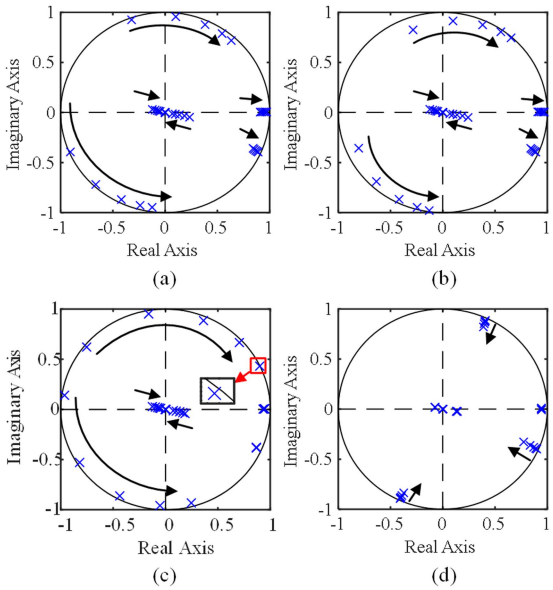

Fig. 9. Pole maps of the closed-loop system with the plant parameters L_1, L_2, C, and R varying from 30% to 300% with f_e to be 1000 Hz. (a) $0.3L_1$ to $3L_1$. (b) $0.3L_2$ to $3L_2$. (c) $0.3C$ to $3C$. (d) $0.3R$ to $3R$.

D. Design Results

To further validate the theoretical analysis of parameter selection, a Bode diagram of the designed open-loop system was drawn in Fig. 8. The graph demonstrates that the algorithm proposed in this article can maintain all phase margins of the system above 65° with the gain margin to be 14.5 dB at 1000 Hz electrical frequency and 200 Hz 0 dB crossover frequency. These results align with the previous analysis and indicate the robustness of the proposed control strategy.

V. Robustness Analysis

A. Parameter Sensitivity of the Closed-Loop Stability

The pole maps of the closed-loop system with the plant parameters L_1, L_2, C, and R varying from 0.3 to 3 times their calibrated values are depicted in Fig. 9, with f_e at 1000 Hz.

It can be observed that all the closed-loop poles remain within the unit circle, signifying system stability even amidst significant variations in parameters. Notably, the trends in parameter variations appear similar for L_1, L_2, and C, whereas the system's stability is notably more sensitive to variations in L_2 and C. Conversely, as R increases, the poles gradually converge towards the center of the unit circle, owing to the damping effect that R imparts to the resonance.

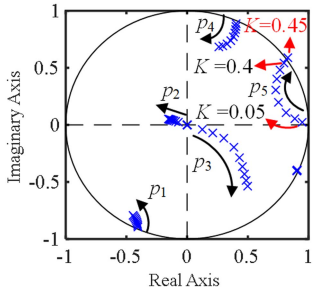

Fig. 10. Root locus with K varying from 0.05 to 0.45.

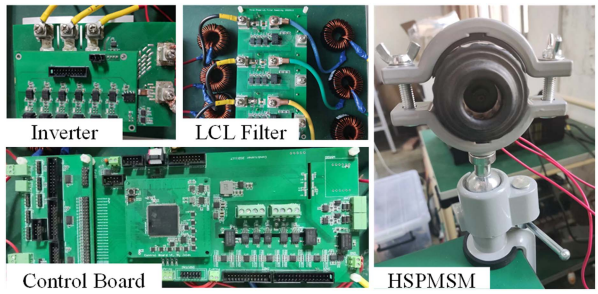

Fig. 11. Schematic diagram of experimental setup.

B. Root Locus

The pole maps of the closed-loop transfer function with the closed-loop gain K varying from 0.05 to 0.45 are depicted in Fig. 10. As K increases, poles p_1 and p_4 gradually converge towards the center of the unit circle, while poles p_2 and p_3 gradually move from the center to the outside of the circle. All poles strictly remain within the unit circle. The system's stability is primarily determined by p_5, which moves towards the center and then progressively shifts outward as K exceeds 0.2. The pole reaches outside the unit circle when $K = 0.45$, indicating a critical value of K at 0.4.

VI. Experiment Validation

To validate the effectiveness of the proposed method, an experimental setup was constructed as shown in Fig. 11. An HSPMSM designed for vacuum cleaners is utilized as the test motor, with its load being directly proportional to the square of the rotational speed. Two three-phase inductors are connected to the ac sampling board in series with the capacitors at the base of the sampling board, forming the *LCL* filter. The control algorithm is executed on a control board based on Texas Instruments high-performance micro-controller unit (MCU) (TMS320F28379D).

In addition, the position of the HSPMSM is acquired using a sensorless method. A Luenberger-style back electromotive force

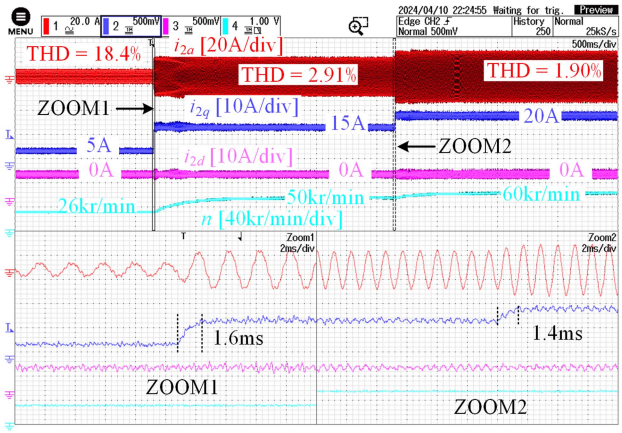

Fig. 12. Current control performance. ($K = 0.05$ and $K_f = 0.1$).

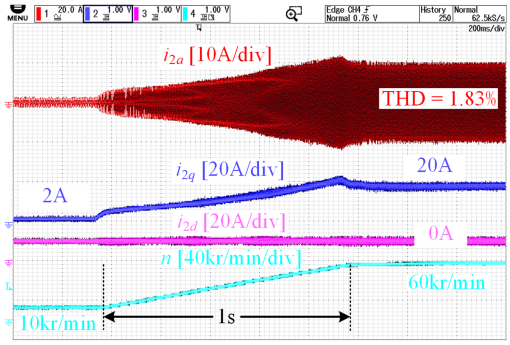

Fig. 13. Speed control performance with slope reference ($K = 0.05$ and $K_f = 0.1$).

observer based on a discrete-time first-order equivalent model is employed to enhance the accuracy of the position estimation, utilizing the capacitor voltage and motor current.

In this section, the dynamic performance, steady-state performance, decoupling performance, and parameter robustness of the system are verified in this section. The parameters of the experimental plant are given in Table I.

Fig. 12 showcases the current control performance with the proposed control strategy. Initially, the q-axis inverter current reference i_{2q}^* steps from 5 to 15 A at 26 kr/min (zoom 1). The q-axis inverter current $i_{2\,q}$ effectively tracks i_{2q}^* with a rise time of 1.4 ms without overshoot and coupling, resulting in a change in the tested motor speed from 26 to 50 kr/min (433 to 833 Hz). In the high-speed region, the current $i_{2\,q}$ steps from 15 to 20 A at 50 kr/min (zoom 2), with a rise time of 1.2 ms. The speed changes from 50 to 60 kr/min then. Notably, no resonance occurs throughout the process.

A. Current Control Performance

Regarding current harmonics, at the low-speed region (26 kr/min), significant harmonics are present due to the dead time effect. However, as the speed rises to 50 kr/min, the harmonics, particularly the fifth and seventh harmonics caused by the dead time effect, are filtered by the *LCL* filter, resulting in a total harmonic distortion of less than 3%.

B. Speed Control Performance

To evaluate the speed control performance, Fig. 13 illustrates the response with a slope speed reference. The speed reference transitions from 10 to 60 kr/min within 1s. The results demonstrate that the speed effectively tracks the reference without oscillations or overshoots, even when employing the sensorless method. Furthermore, no resonance is detected across the entire speed range, demonstrating the effectiveness of the proposed damping method.

C. Robustness Validation

To validate the robustness of the proposed current control strategy, this section conducts a comprehensive investigation into a wide range of control parameter mismatches. The control parameters are primarily determined by three coefficients corresponding to the plant parameters, denoted as

$$\delta = e^{-\frac{R}{L_1+L_2}T}, \lambda \approx \frac{T_s}{L_1+L_2}, \omega_{res} = \sqrt{\frac{L_1+L_2}{L_1L_2C}}. \quad (41)$$

Accordingly, three sets of experiments are conducted with varying parameter mismatches in the digital controller. The mismatched parameters including $\hat{R}$, $\hat{L}_{\text{sum}} = \hat{L}_1 + \hat{L}_2$, $\hat{C}$.

In general, the system is stable under all test conditions. The steady-state performances of all test conditions are nearly consistent, while differences are observed in the dynamic response due to parameter variations.

The first set of experiments, illustrated in Fig. 14, evaluates robustness with coefficient δ variation, with $\hat{R}$ ranging from 0.3 to 3 times its real value. The variation of δ directly impacts the accuracy of zero pole cancellation in the discrete-time PI controller, potentially affecting the decoupling performance of the controller. The dynamic performance is marginally influenced by variations in δ. When the control parameter $\hat{R}$ is smaller than its actual value, the dynamic performance appears unaffected. However, as $\hat{R}$ exceeds the actual value, the coupling is detected in the dynamic response of the d-axis current, indicating the sensitivity of the system to higher values of $\hat{R}$.

In Fig. 15, robustness with variations in all three parameters was evaluated, with inductors L_1 and L_2 simultaneously ranging from 0.3 to 3 times their actual values. As demonstrated in the previous results, the variations of δ and ω_{res} have a negligible influence on control performance. However, the variation in λ may yield different outcomes. Since λ is directly in series with the closed-loop gain K, it will further impact the decoupling capability of the feedforward controller. The experimental results are consistent with the analysis. In Fig. 15, when L_1 and L_2 are smaller than their actual values, the dynamic response significantly deteriorates, and substantial coupling occurs, primarily resulting from low equivalent closed-loop gain and the mismatch of δ. Conversely, when L_1 and L_2 exceed their actual values, the dynamic response markedly accelerates, achieving a rise time as low as 0.8 ms at a 3-times parameter variation.

Finally, in Fig. 16, the robustness with coefficient ω_{res} variation was assessed, with the filter capacitor C ranging from 0.3 to 3 times its actual value. In the controller design, the

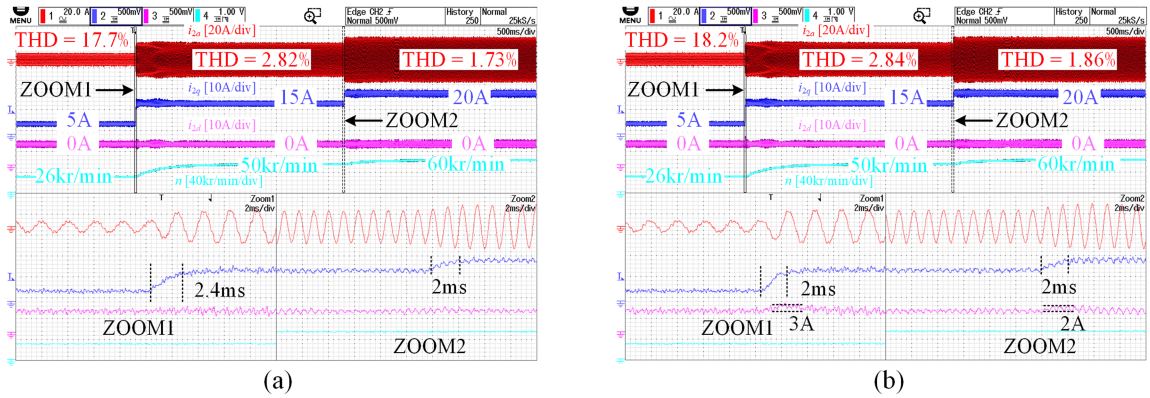

Fig. 14. Current control performance with *R* mismatches ($\boldsymbol{K} = 0.05$, $\boldsymbol{K_f} = 0.1$). (a) $\hat{\boldsymbol{R}} = 0.3\boldsymbol{R}$. (b) $\hat{\boldsymbol{R}} = \boldsymbol{3R}$.

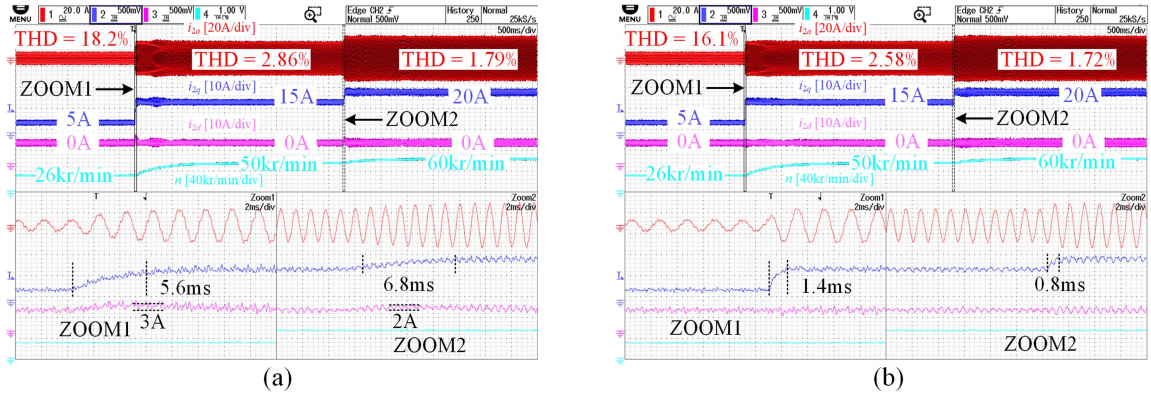

Fig. 15. Current control performance with *L* mismatches ($\boldsymbol{K} = 0.05$, $\boldsymbol{K_f} = 0.1$). (a) $\hat{\boldsymbol{L}}_{\boldsymbol{sum}} = 0.3\boldsymbol{L}_{\boldsymbol{sum}}$. (b) $\hat{\boldsymbol{L}}_{\boldsymbol{sum}} = \boldsymbol{3L}_{\boldsymbol{sum}}$.

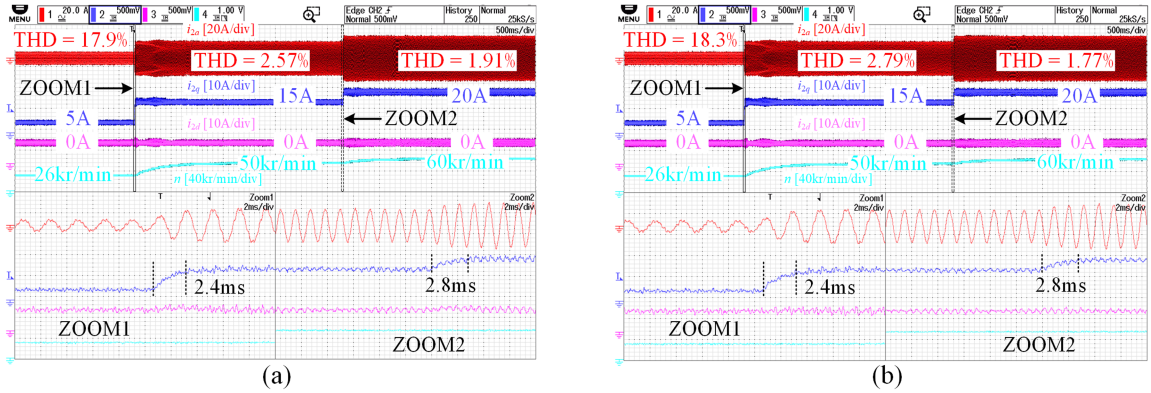

Fig. 16. Current control performance with *C* mismatches ($\boldsymbol{K} = 0.05$, $\boldsymbol{K_f} = 0.1$). (a) $\hat{\boldsymbol{C}} = 0.3\boldsymbol{C}$. (b) $\hat{\boldsymbol{C}} = \boldsymbol{3C}$.

resonance frequency ω_{res} primarily determines the phase lag value of the phase compensator. Therefore, the dynamic and steady performance is minimally affected by the mismatch of ω_{res}, as long as the system remains stable. This inference is validated by the experimental results.

In conclusion, the proposed methods exhibit robustness across a broad range, with all parameters varying from 0.3 to 3 times their actual values. The control performance of the proposed methods demonstrates insensitivity to variations in winding resistance *R* and the filter capacitor *C*, while showing relatively greater sensitivity to variations in the sum of L_1 and L_2 due to changes in the equivalent closed-loop gain.

D. Comparison With Existing Active Damping Methods

To demonstrate the superior robustness of the proposed method, a comparison with recently proposed AD approaches for *LCL*-HSPMSM systems, aimed at enhancing robustness, is

TABLE II
COMPARISON WITH RECENTLY PROPOSED APPROACHES FOR *LCL*-HSPMSM SYSTEMS

	Stable Region with Controller Parameter Mismatches				f_s/f_e	Current Feedback	Overshoot	Rising Time
	$\hat{R}/R$	$\hat{L}_1/L_1$	$\hat{L}_s/L_s$	$\hat{C}/C$				
Proposed Method	0.3~3	$\hat{L}_{sum}/L_{sum}=0.3\sim3$		0.3~3	15	Motor Current	0%	1.6 ms
Yao et al. [31]	×	0.5~1.5	0.5~1.5	0.6~1.4	15.8	Inverter Current	25%	2 ms
Yao et al. [20]	0.5~2	$\hat{L}_{sum}/L_{sum}=0.5\sim1.5$		×	12	Motor Current	25%	2 ms
Yao et al. [32]	×	×	0~2	×	16.7	Motor Current	24%	2 ms
Zhou et al. [16]	0.5~1.5	0.8~1.2	0.35~1.9	0.8~1.2	16.5	Motor Current	30%	2 ms

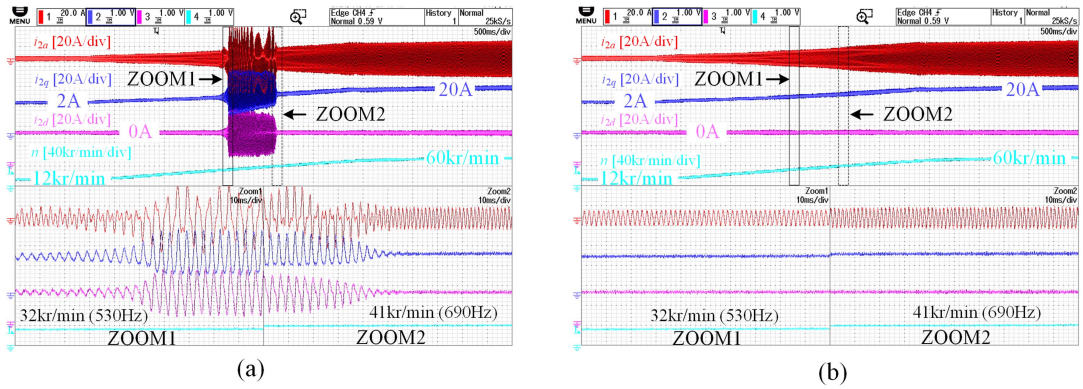

Fig. 17. Comparison with method in [20] of Current control performance with a speed slope reference under parameter mismatches. (a) Dynamic-decoupled current controller in [20] with parameter mismatches $\hat{L}_{\rm sum}=\ 1.7L_{\rm sum}$. (b) Proposed method with parameter mismatches $\hat{L}_{\rm sum}=1.7\ L_{\rm sum}$.

given in Table II. The proposed method exhibits significantly stronger robustness against parameter mismatch with no obvious overshooting observed in the experimental results. Moreover, compared with other methods, the dynamic response of the proposed method is further improved by the relatively high gain of the feedforward controller.

Furthermore, to illustrate the resonance issues at the negative resonance frequency, the current control performance of the method in [20] with parameters mismatches $\hat{L}_{\rm sum}=\ 1.7L_{\rm sum}$ is presented in Fig. 17. It can be observed that the current waveform using the method in [20] begins to oscillate when the electrical frequency exceeds 530 Hz and stabilizes at 690 Hz, while the proposed method remains stable in the whole speed region. This observation can be traced to the Bode diagram in Fig. 18, which showcases the frequency response of the whole open-loop transfer function $G_{\rm open}(z)$ of [20] and the notch filter $G_{\rm notch}(z)$. In [20], a notch filter is used to provide a phase lag at $f_{\rm res+}$, while the phase characteristics in $f_{\rm res-}$ is neglected. Typically, the notch frequency is set as $f_{\rm notch}\ =\ 1.4\ \hat{f}_{\rm res}\ =\ 4026$ Hz, while the true value of the resonance frequency is $f_{\rm res}\ =\ 3736$ Hz. As the result, when the electrical frequency f_e rises to around 600 Hz, the negative resonance frequency $f_{\rm res-}$ rises to 4336 Hz and surpasses the notch frequency, leading to a sharp phase lag in $f_{\rm res-}$, causing system instability. Further, when f_e surpasses 700 Hz, the phase lag in $f_{\rm res-}$ caused by the notch filter gradually decreases, and the system regains stability.

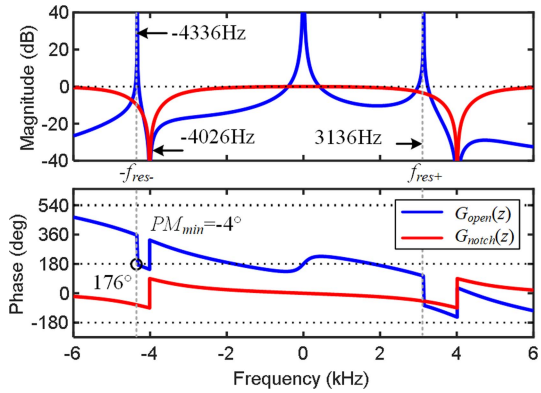

Fig. 18. Bode diagram of the method in [20] with $\hat{L}_{\rm sum}=\ 1.7L_{\rm sum}$ and $f_e=$ 600 Hz.

VII. CONCLUSION

This article identifies the influence of the potential negative resonance frequency of the *LCL*-HSPMSM system within the SRF, which has been commonly overlooked in previous studies. Based on this analysis, a robust 2DOF current control strategy has been proposed. As the main contribution, the resonance issue at both resonance frequencies is effectively damped by the proposed phase compensator and phase gain. The additional coupling caused by the damping methods is addressed by a

feedforward controller. Theoretical analysis and experimental verification have demonstrated that the proposed control strategy exhibits strong robustness against parameter mismatches while achieving satisfactory dynamic performance. The system remains stable even with parameter variations ranging from 0.3 to 3 times the nominal values.

REFERENCES

[1] J. Dannehl, C. Wessels, and F. W. Fuchs, "Limitations of voltage-oriented PI current control of grid-connected PWM rectifiers with LCL filters," *IEEE Trans. Ind. Electron.*, vol. 56, no. 2, pp. 380–388, Feb. 2009.

[2] W. Wu, Y. Liu, Y. He, H. S.-H. Chung, M. Liserre, and F. Blaabjerg, "Damping methods for resonances caused by LCL-Filter-Based current-controlled grid-tied power inverters: An overview," *IEEE Trans. Ind. Electron.*, vol. 64, no. 9, pp. 7402–7413, Sep. 2017.

[3] S. Zhang, S. Jiang, X. Lu, B. Ge, and F. Z. Peng, "Resonance issues and damping techniques for grid-connected inverters with long transmission cable," *IEEE Trans. Power Electron.*, vol. 29, no. 1, pp. 110–120, Jan. 2014.

[4] G. Shen, X. Zhu, J. Zhang, and D. Xu, "A new feedback method for PR current control of LCL-filter-based grid-connected inverter," *IEEE Trans. Ind. Electron.*, vol. 57, no. 6, pp. 2033–2041, Jun. 2010.

[5] C. Citro, P. Siano, and C. Cecati, "Designing inverters' current controllers with resonance frequencies cancellation," *IEEE Trans. Ind. Electron.*, vol. 63, no. 5, pp. 3072–3080, May 2016.

[6] Y. He, X. Wang, D. Pan, X. Ruan, and G. Su, "An ignored culprit of harmonic oscillation in *LCL*-Type grid-connected inverter: Resonant pole cancelation," *IEEE Trans. Power Electron.*, vol. 36, no. 12, pp. 14282–14294, Dec. 2021.

[7] S. G. Parker, B. P. McGrath, and D. G. Holmes, "Regions of active damping control for LCL filters," *IEEE Trans. Ind. Appl.*, vol. 50, no. 1, pp. 424–432, Jan. 2014.

[8] C. Bao, X. Ruan, X. Wang, W. Li, D. Pan, and K. Weng, "Step-by-step controller design for LCL-type grid-connected inverter with capacitor–current-feedback active-damping," *IEEE Trans. Power Electron.*, vol. 29, no. 3, pp. 1239–1253, Mar. 2014.

[9] D. Pan, X. Ruan, C. Bao, W. Li, and X. Wang, "Capacitor-current-feedback active damping with reduced computation delay for improving robustness of LCL-type grid-connected inverter," *IEEE Trans. Power Electron.*, vol. 29, no. 7, pp. 3414–3427, Jul. 2014.

[10] X. Wang, F. Blaabjerg, and P. C. Loh, "Virtual RC damping of LCL-filtered voltage source converters with extended selective harmonic compensation," *IEEE Trans. Power Electron.*, vol. 30, no. 9, pp. 4726–4737, Sep. 2015.

[11] Y. He, X. Wang, X. Ruan, D. Pan, X. Xu, and F. Liu, "Capacitor-current proportional-integral positive feedback active damping for *LCL*-type grid-connected inverter to achieve high robustness against grid impedance variation," *IEEE Trans. Power Electron.*, vol. 34, no. 12, pp. 12423–12436, Dec. 2019.

[12] J. Dannehl, F. W. Fuchs, and P. B. Thøgersen, "PI state space current control of grid-connected PWM converters with LCL filters," *IEEE Trans. Power Electron.*, vol. 25, no. 9, pp. 2320–2330, Sep. 2010.

[13] Z. Zhu, J. Deng, H. Ouyang, and X. Dou, "Optimized sampling mechanism for full-state feedback current control of LCL-equipped high-speed PMSMs for fuel cell air compressor," *IEEE Trans. Transp. Electrific.*, vol. 9, no. 2, pp. 3386–3397, Jun. 2023.

[14] J. Kukkola, M. Hinkkanen, and K. Zenger, "Observer-based state-space current controller for a grid converter equipped with an LCL Filter: Analytical method for direct discrete-time design," *IEEE Trans. Ind. Appl.*, vol. 51, no. 5, pp. 4079–4090, Sep./Oct. 2015.

[15] C. Cheng, S. Xie, Q. Qian, J. Lv, and J. Xu, "Observer-based single-sensor control schemes for LCL-filtered grid-following inverters," *IEEE Trans. Ind. Electron.*, vol. 70, no. 5, pp. 4887–4900, May 2023.

[16] J. Zhou, Y. Yao, Y. Huang, and F. Peng, "Motor current feedback-only active damping controller with high robustness for LCL-equipped high-speed PMSM," *IEEE Trans. Power Electron.*, vol. 38, no. 7, pp. 8707–8718, Jul. 2023.

[17] J. Dannehl, M. Liserre, and F. W. Fuchs, "Filter-based active damping of voltage source converters with *LCL* filter," *IEEE Trans. Ind. Electron.*, vol. 58, no. 8, pp. 3623–3633, Aug. 2011.

[18] J. Wang, J. D. Yan, L. Jiang, and J. Zou, "Delay-dependent stability of single-loop controlled grid-connected inverters with LCL filters," *IEEE Trans. Power Electron.*, vol. 31, no. 1, pp. 743–757, Jan. 2016.

[19] W. Yao, Y. Yang, X. Zhang, F. Blaabjerg, and P. C. Loh, "Design and analysis of robust active damping for LCL filters using digital notch filters," *IEEE Trans. Power Electron.*, vol. 32, no. 3, pp. 2360–2375, Mar. 2017.

[20] Y. Yao, Y. Huang, F. Peng, J. Dong, and Z. Zhu, "Discrete-time dynamic-decoupled current control for *LCL*-equipped high-speed permanent magnet synchronous machines," *IEEE Trans. Ind. Electron.*, vol. 69, no. 12, pp. 12414–12425, Dec. 2022.

[21] Y. Yao, Y. Huang, F. Peng, J. Dong, and Z. Zhu, "A general single-sensor damping framework for LCL-equipped high-speed PMSM drives," *IEEE Trans. Power Electron.*, vol. 70, no. 5, pp. 5375–5380, May 2023.

[22] M. Seilmeier and B. Piepenbreier, "Sensorless control of PMSM for the whole speed range using two-degree-of-freedom current control and HF test current injection for low-speed range," *IEEE Trans. Power Electron.*, vol. 30, no. 8, pp. 4394–4403, Aug. 2015.

[23] Z. Pan, F. Dong, J. Zhao, L. Wang, H. Wang, and Y. Feng, "Combined resonant controller and two-degree-of-freedom PID Controller for PMSLM current harmonics suppression," *IEEE Trans. Ind. Electron.*, vol. 65, no. 9, pp. 7558–7568, Sep. 2018.

[24] S. Lin, Y. Cao, Z. Wang, Y. Yan, T. Shi, and C. Xia, "Speed controller design for electric drives based on decoupling two-degree-of-freedom control structure," *IEEE Trans. Power Electron.*, vol. 38, no. 12, pp. 15996–16009, Dec. 2023.

[25] H. A. A. Awan, S. E. Saarakkala, and M. Hinkkanen, "Flux-linkage-based current control of saturated synchronous motors," *IEEE Trans. Ind. Appl.*, vol. 55, no. 5, pp. 4762–4769, Sep./Oct. 2019.

[26] H. A. Hussain, "Tuning and performance evaluation of 2DOF PI current controllers for PMSM drives," *IEEE Trans. Transp. Electrific.*, vol. 7, no. 3, pp. 1401–1414, Sep. 2021.

[27] M. A. Awal, L. D. Flora, and I. Husain, "Observer based generalized active damping for voltage source converters with LCL filters," *IEEE Trans. Power Electron.*, vol. 37, no. 1, pp. 125–136, Jan. 2022.

[28] H. Kim, M. W. Degner, J. M. Guerrero, F. Briz, and R. D. Lorenz, "Discrete-time current regulator design for AC machine drives," *IEEE Trans. Ind. Appl.*, vol. 46, no. 4, pp. 1425–1435, Jul./Aug. 2010.

[29] A. G. Yepes, F. D. Freijedo, J. Doval-Gandoy, Ó. López, J. Malvar, and P. Fernandez-Comesaña, "Effects of discretization methods on the performance of resonant controllers," *IEEE Trans. Power Electron.*, vol. 25, no. 7, pp. 1692–1712, Jul. 2010.

[30] F. Briz, M. W. Degner, and R. D. Lorenz, "Analysis and design of current regulators using complex vectors," *IEEE Trans. Ind. Appl.*, vol. 36, no. 3, pp. 817–825, May/Jun. 2000.

[31] Y. Yao, D. Xu, Y. Chen, F. Peng, and Y. Huang, "Robust notch filter-based active damping design for LCL-equipped high-speed PMSMs considering dual resonance problem," *IEEE Trans. Ind. Electron.*, vol. 71, no. 11, pp. 13845–13854, Nov. 2024.

[32] Y. Yao, Y. Huang, F. Peng, J. Dong, and Z. Zhu, "Dynamic-decoupled active damping control method for improving current transient behavior of LCL-equipped high-speed PMSMs," *IEEE Trans. Power Electron.*, vol. 37, no. 3, pp. 3259–3271, Mar. 2022.

Longhao Shi received the B.Sc. degree in electrical engineering in 2022 from Southeast University, Nanjing, China, where he is currently working toward the M.Sc. degree in electric engineering with the School of Electrical Engineering, Southeast University. His research interests include the control of high-speed drive systems.

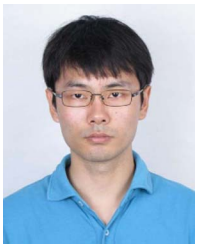

Chenwen Cheng received the B.S. and Ph.D. degrees from Zhejiang University, Hangzhou, China, in 2012 and 2017, respectively, both in electrical engineering.

From 2018 to 2021, he was a Postdoc Researcher with San Diego State University, San Diego, CA, USA. He is currently with Southeast University, Nanjing, China. His research interests include motor control, renewable power generation, and wireless power transfer technologies.

Mingjin Hu (Member, IEEE) was born in Jiangxi, China, in 1994. He received the B.Sc. and Ph.D. degrees in electrical engineering from the School of Electrical Engineering, Southeast University, Nanjing, China, in 2016 and 2023, respectively.

His current research interests include the modeling and advanced control of electrical drives.

Wei Hua (Senior Member, IEEE) received the B.Sc. and Ph.D. degrees in electrical engineering from Southeast University, Nanjing, China, in 2001 and 2007, respectively.

From 2004 to 2005, he was with the Department of Electronics and Electrical Engineering, The University of Sheffield, U.K., as a Joint-Supervised Ph.D. Student. His teaching and research interests include design, analysis, and control of electrical machines, especially for PM brushless machines and switching reluctance machines, etc.

Chunyu Lu received the B.Sc. and M.Sc. degrees in electrical engineering from Southeast University, Nanjing, Jiangsu, China, in 2020 and 2023, respectively.

He is currently with the State Grid Changzhou Electric Power Supply Company, Lanzhou, China. His main research interests include the discrete control of high-speed permanent magnet synchronous machines and grid integration of new energy equipped with *LCL* filters.